Onset of Rayleigh-Bénard convection in cylindrical containers

François Hébert,[1] Ryan Hufschmid,[1] Janet Scheel,[2] and Guenter Ahlers[1]
[1]*Department of Physics, University of California, Santa Barbara, California 93106, USA*
[2]*Department of Physics, Occidental College, 1600 Campus Road, M21, Los Angeles, California 90041, USA*
(Received 9 January 2010; published 28 April 2010)

We determined the critical Rayleigh numbers Ra_c for the onset of convection in cylindrical containers with aspect ratios $1 \lesssim \Gamma \equiv D/L \lesssim 9$ (D is the diameter and L the height) and the patterns that form just above Ra_c, both from experiment and by direct numerical simulation (DNS). Results for Ra_c agree well with the linear stability analysis by Buell and Catton for containers with finite sidewall conductivity. For $\Gamma \leq 1.58 \pm 0.10$, we found that the patterns correspond to an azimuthal Fourier mode with mode number $m=1$, corresponding to a single convection roll. For $1.58 \lesssim \Gamma \lesssim 3.26 \pm 0.02$, the pattern was a concentric roll, corresponding to $m=0$. For $3.26 \leq \Gamma \lesssim 4$, an $m=1$ mode was found again, but near $\Gamma=4$ either $m=1$ or $m=2$ was observed in different runs. These results are consistent with the marginal stability curves calculated by Buell and Catton in the sense that the mode that is the first as a function of Ra to acquire a positive growth rate is the one that is observed. For $\Gamma \gtrsim 4$, the theoretical marginal curves for the four lowest modes lie very close together. There we found patterns near onset that corresponded to various modes, including $m=2$ and 4. At relatively large $\Gamma \gtrsim 6$, we observed parallel straight rolls quite close to onset. Our patterns agree with several DNS investigations by others, but at some Γ values differ from those observed experimentally by Stork and Müller. Some results for the pattern evolution with increasing Ra are reported as well.

DOI: 10.1103/PhysRevE.81.046318 PACS number(s): 47.54.−r, 47.20.Bp

I. INTRODUCTION

From experiment, it has been known for long that convection occurs in a plane-parallel horizontal fluid layer heated from below (Rayleigh-Bénard convection or RBC) when the temperature difference ΔT across the sample exceeds some critical value ΔT_c [1–3]. The onset occurs when the dimensionless parameter

$$\mathrm{Ra} = \frac{\alpha g L^3 \Delta T}{\kappa \nu}, \tag{1}$$

which represents the strength of the driving by the thermal gradient, reaches a critical value Ra_c [4,5]. In Eq. (1), α is the thermal-expansion coefficient, g is the gravitational acceleration, L is the thickness of the fluid layer, κ is the thermal diffusivity, and ν is the kinematic viscosity. The parameter Ra, apparently first introduced by Lorenz [6] (see also the first footnote of Ref. [7]), but generally attributed to Rayleigh [4], is now known as the Rayleigh number. For a sample of infinite lateral extent and with rigid isothermal boundary conditions at the top and bottom plates, the value of Ra_c was calculated by Jeffreys [5] and found to be 1708. Experimental confirmation of this result with high accuracy is nontrivial since, in addition to an accurate experimental measurement of ΔT_c, all relevant fluid properties and especially the sample thickness have to be known well. Under most favorable circumstances, experiment has reproduced the predicted value within a few percent (see, for instance, Fig. 17 of [8]). Rayleigh and Jeffreys also predicted that the bifurcation is of the stationary type, i.e., that the relevant eigenvalues are real. This, too, agrees with many experiments [3].

When $\mathrm{Ra} > \mathrm{Ra}_c$, convective flows form a pattern and contribute to the heat transport. Here, especially interesting issues arise. The first pertains to the nature of the bifurcation to convection. Again, for rigid top and bottom boundaries, it was predicted by Schlüter *et al.* [9] that the bifurcation is supercritical. This was confirmed with high resolution by numerous experiments. In the left part of Fig. 1, we show high-resolution data for the ratio between the effective thermal conductivity in the presence of convection and the conductivity of the quiescent sample, which is known as the Nusselt number, Nu. The measurements were made in a sample of large, but of course necessarily finite, lateral extent. The open symbols were taken with increasing and the solid ones with decreasing ΔT. The results reveal no hysteresis and show that the convective heat-transport contribution grows continuously and linearly from zero as ΔT exceeds ΔT_c. Both of these findings are in agreement with the prediction [9].

The second interesting aspect of RBC is the nature of the convection patterns that form above onset. In principle, pat-

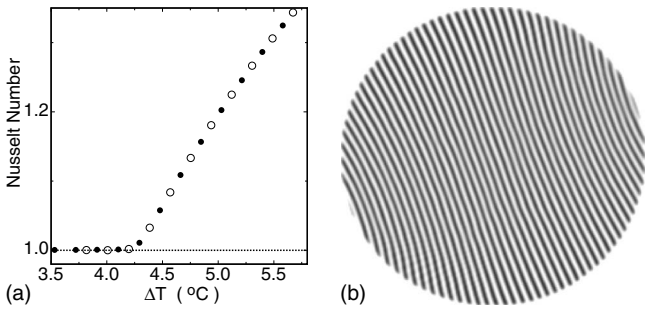

FIG. 1. (Left) Nusselt number measurements using ethanol in a circular cell with $L=1.54$ mm and diameter $D=88$ mm. Open (closed) circles: increasing (decreasing) ΔT. (Right) Near-perfect pattern of parallel convection rolls for $\Delta T \simeq 1.2 \Delta T_c$ (from [10]). The convecting section had a diameter of $D=3.18$ cm and a thickness of $L=0.075$ cm and the fluid was compressed sulfur hexafluoride.

terns of parallel straight rolls, of squares, or of hexagons could form periodic structures in the plane. Here again, theory predicts [9] that only the straight-roll case is stable when ΔT_c is sufficiently small so that the temperature dependence of the fluid properties may be neglected. This too has been confirmed by numerous experiments [3], although in most cases the roll patterns tend to be rendered imperfect by the presence of side walls. In the right part of Fig. 1, we show a nearly perfect example. It was obtained in a sample with uniform spacing L_0 between the plates out to a radius r_0 and with a gradually decreasing spacing $L(r)$ beyond r_0 which continuously and smoothly reduced Ra (see Eq. (1)) to values below Ra_c and thereby essentially eliminated the sidewall influence.

From the above discussion, one sees that much is known about the nature of RBC, at least not too far from onset, when the sample is of large lateral extent and the influence of the side walls can be neglected. The present paper is a contribution to our knowledge about convection in finite containers, where our understanding is far less complete and where the side walls can have a decisive influence on the nature of the bifurcation and on the patterns that form above it. Of exceptional interest have been the cases of elliptical and stadium-shaped side walls which, depending on circumstances, yielded parallel rolls, convex disclinations, and a defect combination known as protuberances [11,12]. Here, however, we shall focus on the case where the samples are cylindrical with a circular cross section. Extensive experimental studies have been reported for samples of modest to large aspect ratio

$$\Gamma \equiv D/L \tag{2}$$

(D is the cylinder diameter). Some of these led to concentric roll patterns [13], but these are believed to be forced by radial temperature gradients near the side wall due to the particular cell construction. Others led to parallel-roll patterns near onset, with various degrees of disorder introduced by the side walls and greater complexity evolving as Ra and Γ were increased (see, for instance, [3,14–21]).

Here we shall consider cylindrical samples with small aspect ratios $\Gamma \lesssim 9$. These cases were studied experimentally in a seminal investigation by Stork and Müller (SM) [22] and our work has some overlap with and is an extension of theirs. They determined Ra_c as a function of Γ. Depending on Γ, these authors found a variety of patterns above but close to Ra_c. At small $\Gamma \lesssim 1.6$, these included an unstable nonaxisymmetric single convection roll corresponding to an azimuthal Fourier mode with $m=1$ which (at least in the range $1.05 \lesssim \mathrm{Ra}/\mathrm{Ra}_c \lesssim 1.1$) in time transformed to an $m=2$ mode, an axisymmetric roll corresponding to $m=0$ over the intermediate range $1.8 \lesssim \Gamma \lesssim 3.2$, and parallel rolls at larger Γ. Another relevant experimental study is that of Kirchartz *et al.* [14], who found that parallel rolls were formed under quasistatic conditions for $\Gamma=6$ and 6.8. A wide range of small to very small aspect ratios was investigated experimentally by Müller *et al.* [23] who found a nonaxisymmetric ($m=1$) mode for $0.28 \lesssim \Gamma \lesssim 1$ and an axisymmetric ($m=0$) mode for $\Gamma=2$. Although an interesting qualitative picture has emerged from these experimental studies, quantitative information about the Γ ranges of stability of the various patterns is still lacking. Further, the observations [22] of $m=2$ for $\Gamma \simeq 1.6$ and of parallel rolls for Γ as small as 3.2 are unexpected. If these patterns did indeed form immediately above onset, then they are inconsistent with the linear stability analysis [24] and a supercritical bifurcation. In any case, they are at odds with the results that we shall report below.

An interesting issue has been the question of possible multistability of different patterns under identical external conditions but different histories. This was addressed experimentally by Hof *et al.* [25], who were able to generate numerous different patterns in a sample with $\Gamma=4$ at constant values of Ra well above Ra_c. In contrast, close to onset, one would presume that the pattern will be unique except perhaps near codimension-two points where the pattern changes discontinuously as a function of Γ; but only very little is known about this from experiment.

Cylindrical samples of fairly small Γ also have been addressed by several theoretical investigations. In the early work of Charlson and Sani, Ra_c was determined as a function of Γ from a linear stability analysis (LSA) for both conducting and insulating boundary conditions (BCs) at the lateral walls and rigid isothermal BCs at the top and bottom [26,27]. In a later paper, these authors used a Galerkin method to study the nonlinear nature of axisymmetric patterns just above onset [28], but this work did not allow for a breaking of the rotational invariance. The LSA was extended by Buell and Catton [24] who used rigid isothermal BCs at the top and bottom and included the effect of finite side-wall conductivity. For insulating sidewalls, the results of Buell and Catton were confirmed by the LSA of Wanschura *et al.* [29]. Similarly, the values of $\mathrm{Ra}_c(\Gamma)$ for both insulating and conducting sidewalls by Hardin *et al.* [30] agree with the BC calculations. Since the Buell and Catton analysis with finite sidewall conductivity corresponds most closely to the experimental system, we shall use its results for comparison to our measurements.

In more recent times, the development of greater computing power encouraged direct numerical simulations (DNSs) as well as more extensive Galerkin calculations of the patterns in cylinders of various aspect ratios and side-wall conductivities, both near onset and further above it [23,29,31–39]. Especially, the recent work by Borońska and Tuckerman [38,39] provided a very detailed picture of the complicated array of primary and secondary bifurcations that occur as Ra is increased well above onset for the case $\Gamma=4$ and Prandtl number $\mathrm{Pr} \equiv \nu/\kappa = 6.7$. That Prandtl number was chosen to be equal to that of the experiment by Hof *et al.* [25] so that a direct comparison could be attempted.

In the present paper, we focus on the region close to and somewhat above onset and present measurements as well as DNS over the range $1 \leq \Gamma \leq 9$. For our fluid and our DNS, Pr was equal to 29. It is well known that, for a given bifurcating mode, $\mathrm{Ra}_c(\Gamma)$ is independent of Pr. For a supercritical bifurcation and slightly above onset, we expect the pattern that forms to be the one that corresponds to the mode with the smallest Ra_c because there is no other. Thus, the pattern first observed above Ra_c (albeit not necessarily its amplitude) should also be independent of Pr and it is meaningful to compare our experimental or DNS observations to those

based on measurements or calculations at various values of Pr. We shall do this in more detail below in Sec. III. However, further above onset and particularly near secondary bifurcations, a dependence on Pr is expected and direct comparison to other work would be quantitatively meaningful only when the Prandtl number is the same.

In addition to $\mathrm{Ra}_c(\Gamma)$, we also determined the patterns and their overall intensity slightly above onset. In the experiment, the variance of shadowgraph images was measured as a function of ΔT; in the DNS, the Nusselt number Nu was determined from the temperature and velocity fields. These measurements or computations were consistent with a supercritical bifurcation in the sense that σ^2 or Nu grew continuously and linearly from its pure-conduction value as ΔT exceeded ΔT_c.

For the patterns close to onset, we found an interesting sequence as a function of Γ from a nonaxisymmetric single convection roll (corresponding to $m=1$) at the smallest Γ to an axisymmetric roll (corresponding to $m=0$) at intermediate Γ and to more complex patterns (with $m=1$, 2, 4, as well as less symmetric modes) at larger Γ. Our results were sufficiently closely spaced as a function of Γ to determine the locations of the codimension-two points that bracket the $m=0$ state to be $\Gamma_{\mathrm{CD2}}^{(1)}=1.58\pm0.10$ and $\Gamma_{\mathrm{CD2}}^{(2)}=3.26\pm0.02$. These results agree reasonably well, but not perfectly, with the LSA of Buell and Catton [24].

Where there is overlap, several but not all of our patterns agree with those observed in the experiments of Stork and Müller [22] who worked over the range $1.6\lesssim\Gamma\lesssim6.4$. At large $\Gamma\simeq6$, our results agree with the experimental observation of straight rolls by Kirchartz *et al.* [14] They are also consistent with the experimental findings of Müller *et al.* [23], for Γ near 1 and 2. As will be discussed in more detail below, our results also are consistent with, but more detailed than, a number of DNS investigations.

To a more limited extent, we present also the pattern evolution at constant Γ as ΔT was increased further above ΔT_c. For aspect ratios near 4, those results are qualitatively consistent with several aspects of the DNS by Borońska and Tuckerman [39] for Pr=6.7.

In Sec. II, we discuss the experimental apparatus, the properties of the fluid that was used in the experiment, our methods of shadow-graph image analysis, and the experimental protocol used in the data acquisition. In Sec. III A, we present the results for the variance of the images and show our method of extracting Ra_c. There we also show the results for the dependence of Ra_c on Γ. In Sec. III B, we show images of the observed patterns for various Γ and at small $\varepsilon\equiv\Delta T/\Delta T_c-1$, while the pattern evolution at somewhat larger ε is discussed in Sec. III C. Section IV presents the results of the DNS. The paper finishes with a brief summary in Sec. V.

II. EXPERIMENT

A. Apparatus

The Rayleigh-Bénard convection apparatus was described in detail before [40]. The bottom plate was a polished silver disk with a metal-film heater fixed to its lower surface. The top plate was a sapphire disk, over which temperature-controlled cooling water was circulated. The sample was sandwiched directly between these two plates. To obtain the desired temperature difference $\Delta T=T_b-T_t$ across the sample, we fixed the temperatures T_t and T_b at the top and bottom of the sample at values that maintained a mean temperature $T_m\equiv(T_t+T_b)/2$ of 40.00 °C.

The convection patterns were visualized using the shadowgraph method [8]. Measurements were made with three different sets of cells. Each set consisted of a single Lexan plate (conductivity $\lambda_w\simeq0.23$ W/m K) with a diameter just under 10 cm through which several cylindrical holes of different radii were machined to serve as the cells. All cell dimensions are given in Table I. The top view of one of these plates is shown in Fig. 2. In order to permit fluid to enter the cells, the cells were interlinked by very thin channels. We expect that the small size of these channels ensured that no significant flow between cells occurred during the experiment and that the effect on the convection patterns was negligible. The images shown in Figs. 5 and 7–11 below do not show any preferred orientation or deviation from expected symmetries, suggesting that the channels had no significant influence. The spacing between pixels in the images varied somewhat for different sets, but always was much smaller than the sample thickness L. Since patterns generally show spacial variations only on the scale of L or larger, we expect that we resolved all interesting features.

The first wall (henceforth W1a) had a thickness $L=0.217\pm0.003$ cm and in it there were 11 convection cells. These cells had diameters D ranging from 0.40 to 1.93 cm, corresponding to aspect ratios Γ varying from 1.85 to 8.88. The second wall (W1b) provided closer scanning of Γ over the range of 2.2–3.6. It had a thickness $L=0.240\pm0.003$ cm and contained ten cylindrical cells (of which only six were finally used) with diameters ranging from 0.48 to 0.87 cm with corresponding aspect ratios Γ of 1.99–3.61. It was introduced to search for possible hysteresis at onset in this Γ range. The third wall (W2) was designed for closer scanning of Γ at relatively small values. It had a thickness $L=0.476\pm0.003$ cm and contained ten cylindrical cells with diameters ranging from 0.48 to 1.90 cm with corresponding aspect ratios Γ of 1.00–4.00. All actual dimensions are given in Table I.

The uncertainty $\pm\delta L$ of L leads to an uncertainty of $\mp\delta L/L$ for Γ. We find this to be 0.014, 0.013, and 0.006 for W1a, W1b, and W2, respectively. The uncertainty of the cell diameters is similar and thus contributes negligibly for the larger Γ values, but comparably for Γ near one. The actual cell spacing is determined by pressing the bottom metal plate and the top sapphire plate tightly together, with the Lexan plate between them. Thus the actual spacing of the cells may be slightly larger, but not less, than the measured thickness of the Lexan plates. We estimate that this could lead to an additional systematic error of the Γ values not larger than −0.014 for W1a and W1b and −0.006 for W2.

B. Fluid properties

The sample fluid was isopropyl alcohol (propan-2-ol) with a mean temperature of 40.00 °C, where literature

TABLE I. Aspect ratios $\Gamma \equiv D/L$, pattern mode m near onset, diameters D, and critical temperature differences ΔT_c of the sample cells. A question mark in the mode column indicates that a pattern with recognizable symmetry could not be identified. The parameter r indicates that parallel rolls were found, with the number preceding it giving the number of rolls.

	W1a (L=0.217 cm)				W1b (L=0.240 cm)				W2 (L=0.476 cm)			
Cell No.	Γ	m	D (cm)	ΔT_c (K)	Γ	m	D (cm)	ΔT_c (K)	Γ	m	D (cm)	ΔT_c (K)
1	8.88	7r	1.928	1.503					4.00	2	1.905	0.163
2	8.18	7r	1.775	1.540	2.17	?	0.521	1.570	3.66	?	1.745	0.163
3	7.47	6r	1.623	1.549					3.33	1	1.588	0.155
4	6.77	5r	1.471	1.558	2.53	0	0.607	1.430	3.00	0	1.427	0.168
5	6.07	4	1.318	1.572					2.67	0	1.270	0.160
6	5.37	4r	1.166	1.568	2.89	0	0.693	1.390	2.33	0	1.110	0.176
7	4.67	2	1.013	1.601					2.00	0	0.952	0.210
8	3.96	1	0.861	1.636	3.25	0	0.780	1.350	1.66	0	0.792	0.267
9	3.26	1	0.709	1.685	3.43	1	0.823	1.330	1.33	1	0.635	0.324
10	2.56	0	0.555	1.733	3.61	1	0.866	1.310	1.00	1	0.475	0.511
11	1.85	0	0.401	2.233								

values [41] give α=0.00131 K^{-1}, $\kappa=6.11\times10^{-8}$ m^2/s, and $\nu=1.77\times10^{-6}$ m^2/s, yielding $\alpha/(\kappa\nu)=1.21\times10^{10}$ $s^2/(m^4\,K)$ for the combination relevant to the Rayleigh number.

In a previous investigation [42] using a sample with Γ=58 (which is effectively infinite) and an accurately known spacing L, it was shown that values of ΔT_c calculated with these properties are larger than the theoretical value corresponding to Ra_c=1708. At a mean temperature of 32 °C, the results for isopropanol were high by a factor of 1.13. We do not know this factor for our present mean temperature of 40 °C, but we do not expect to be able to reproduce the theoretical Ra_c values very well because of this uncertainty in the fluid properties. Thus, for the comparison to the predicted values of Ra_c, we adjusted all our results for Ra_c by a factor close to unity, chosen so as to give agreement at our largest Γ values with the theoretical results of Ref. [24]. This factor turned out to be 1.07.

Other relevant properties are the thermal conductivity λ=0.132 W/mK and the Prandtl number $Pr \equiv \nu/\kappa$=28.9.

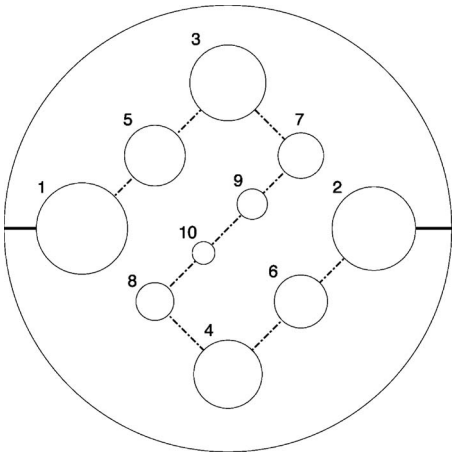

FIG. 2. Layout of the sample cells for side wall W2.

The ratio of the conductivities λ/λ_w was 0.57. The wall admittance $C \equiv [(D/2)\lambda]/(d\lambda_w)$ was not very well defined for our experiment because the wall thickness d varied widely. Our cells had irregularly shaped side walls (see Fig. 2) and thus no unique value of d. Nonetheless, roughly one might choose C somewhere between 1 and 3.

C. Image analysis

A sequence of images taken at $\Delta T < \Delta T_c$ was averaged and used as a background. The subsequent series of images taken with larger ΔT values were also averaged in the same manner. These averaged images were then divided by the background image in order to correct for irregularities in the sample illumination. This divided image was passed through an edge-detection algorithm to determine the positions of the actual samples. Finally, a mask was applied, such that later calculations would only include pixel data from inside the particular cell of interest.

The variance σ^2 (mean-square deviation computed over all background-divided image pixels) was calculated for each cell and each ΔT. It is a quantitative measure of the strength of convection in the sample. Before the onset of convection, an image differs from the background only by random noise and the variance of the divided image is very close to zero. After onset, there is a significant difference between the image and the background and thus σ^2 is significantly larger than zero.

Finally, the images were passed through a Gaussian blur filter to smooth out high-frequency spacial variations not caused by the convection, but for instance by irregularities in the bottom-plate surface and random noise. Then, by rescaling the image to cover a full range of gray values, we obtained images from which it was easier to visually identify pattern types.

D. Experimental procedure

In a given run, ΔT was first set to approximately 3/4 of the estimated critical value ΔT_c for onset and the system was

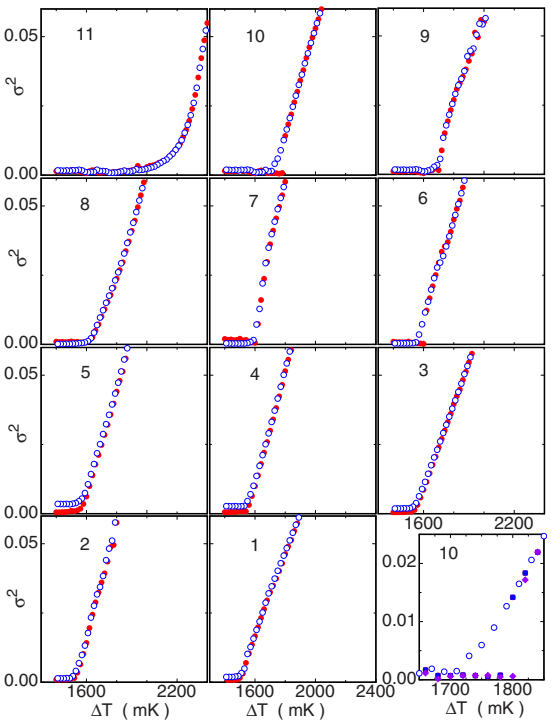

FIG. 3. (Color online) Variance σ^2 of the shadowgraph images as a function of ΔT for sample W1a. The number in the upper left of each figure is the cell number (see Table I). Solid circles (red): ΔT increasing. Open circles (blue): ΔT decreasing. Lower right figure is a detailed view near the bifurcation for cell 10. For this case, three separate runs, each with increasing and decreasing ΔT, were made on different days and gave nearly identical results. Although all three runs with increasing ΔT were plotted, only two of them are distinguishable in the figure.

left to equilibrate for 3 h. A sequence of 256 shadowgraph images of this background (i.e., the sample without any convection) was taken. The temperature difference was then increased in increments of 4 mK for W2 or 10 mK for W1a and W1b, leaving the system to equilibrate for 1–3 h at each step. After each equilibration time, a rapid sequence of 256 images was taken. For the runs with decreasing ΔT, the temperature difference was increased first as described above up to the maximum desired ΔT. After waiting for 1–3 h, ΔT was decreased in the same increments of 4 to 10 mK, waiting 1 h between steps for a stationary state.

III. EXPERIMENTAL RESULTS

A. Onset of convection

Figure 3 shows the variance σ^2 as a function of the applied temperature difference for the cells of sample W1a. The solid (open) circles were obtained with increasing (decreasing) ΔT. For most of the cells, the data reveal a fairly sharp nonhysteretic transition typical of a supercritical bifurcation. However, there are interesting exceptions.

Cell 11, with $\Gamma=1.85$, shows a strongly rounded transition indicative of an imperfect bifurcation, with excellent agreement between data obtained with increasing and decreasing ΔT. The reason for the rounding is not clear; a possible influence of the side-wall conductance comes to mind, but we do not know of a reason why this should be important for cell 11 only and not for nearby aspect ratios such as that of cell 10 with $\Gamma=2.56$.

The data for cells 10 ($\Gamma=2.56$) and 6 ($\Gamma=5.37$) reveal seemingly hysteretic onsets, with a discontinuous jump of σ^2 with increasing and a continuously vanishing σ^2 with decreasing ΔT. The results for cell 10 are shown in more detail in the lower right expanded panel of the figure. There three separate runs are plotted, but the one also shown in the top middle panel is not observable because its data fall directly below those of a second run. One sees that the apparent hysteresis is quite reproducible. Such a signature could be produced by the genuine hysteresis of the stable or metastable states associated with a subcritical or transcritical bifurcation. However, an apparent hysteresis could also occur in a sample with exceptionally perfect geometrical and thermal conditions where the unstable conduction state can persist for many hours.

Observation of hysteresis, apparent or real, caused us to investigate sample W1b where the aspect ratios of the cells are more closely spaced in the vicinity of the aspect ratio of cell W1a-10. We did not observe hysteresis for any of the cells of sample W1b and thus conclude that its observation for W1a-10 and W1a-6 most likely is not genuine but rather due to an exceptional longevity of the conduction state even above ΔT_c where that state is unstable. Data for some of the cells of sample W2 also suggest a jump in σ^2 with increasing ΔT, but the much smaller values of ΔT_c made it impossible for us to actually observe "hysteresis" when ΔT was decreased. In all cases, ΔT_c was taken to be at the intersection of straight lines through the σ^2 results for the conduction state and through those near onset for the convection state.

We compare our results for Ra_c to the LSA by Buell and Catton [24] because these allow for nonaxisymmetric modes and consider the finite conductivity of the side walls; but LSAs for insulating side walls (see, for instance, [24,29]) have yielded results that are similar. Buell and Catton considered the influence of the wall admittance C (see Sec. II B). Our cells had irregularly shaped side walls (see Fig. 2) and thus no unique value of C. Nonetheless, roughly one might choose C somewhere between 1 and 3. We chose the theoretical results for the nearest value $C=3.3$ given in Ref. [24] for comparison to the measurements.

The critical Rayleigh number for each cell was calculated from the measured ΔT_c using initially the literature value of $\alpha/\kappa\nu$. As discussed in Sec. II B, these fluid properties yield values of Ra that are too large by a factor of 1.13 at a mean temperature $T_m=32$ °C [42]. At our $T_m=40°$, this factor has not been measured. Thus, we divided our Ra_c results by a constant that caused agreement with the calculations of Ref. [24] at the larger Γ values of sample W1a where Ra_c has nearly reached the limit where Γ is infinite. The factor needed turned out to be 1.07. After this adjustment, the agreement with the calculation is within 2% for most of our cells. In Fig. 4, we show Ra_c vs. Γ. The left panel gives the data from sample W1a and the right one shows the W2 results. We note that only the result for cell W1a-11, with $\Gamma=1.85$, differed significantly from the calculation. This cell also shows a strongly rounded transition (see Fig. 3) which

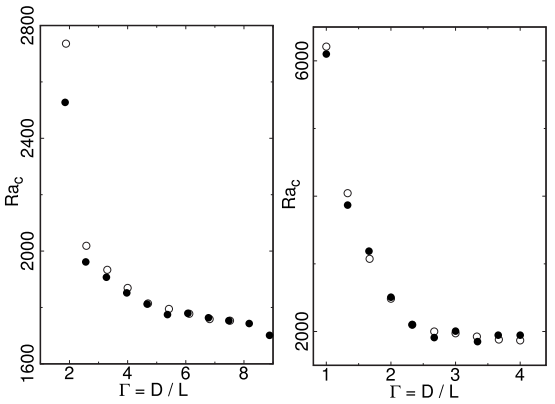

FIG. 4. Critical Rayleigh number Ra_c as a function of Γ. Solid circles: this work. Open circles: calculations from Ref. [24] for a wall admittance $C=3.3$. Left figure shows data from sample W1a and the right figure those from W2.

made a precise determination of ΔT_c difficult. When comparing to the LSA, one should also keep in mind that the theoretical value of R_c^{LSA} can be quite sensitive to the precise value of the side-wall admittance C in some ranges of Γ [24]. Our results, and their agreement with the LSA, confirm and extend the previous measurements and conclusions by Stork and Müller [22].

B. Patterns close to onset

We illustrate the patterns that form at or very near onset with the example of sample W2 as shown in Fig. 5. Even though the physical diameters of the cells differ by as much as a factor of 4, the images have been scaled so that they are of the same size for all Γ. Note that dark (bright) regions in the images correspond to lower (higher) index of refraction and thus to rising (falling) warm (cold) fluid. These patterns are for $\varepsilon \simeq 0.1$, but they are representative also of those observed at smaller ε and for all but the two largest Γ values are likely to be the ones that form directly at the bifurcation point. In the remainder of this section, we shall consider the patterns as a function of Γ starting at small Γ. All our results are summarized in Table I above.

At the smallest $\Gamma=1.00$ and 1.33 [Figs. 5(a) and 5(b) for cells W2–10 and W2–9], one sees that the patterns are described well by an azimuthal Fourier mode with $m=1$. This pattern is referred to as a dipole by Borońska and Tuckerman [39]. At these small Γ values, the $m=1$ mode was found also by our DNS (see Sec. IV below) as well as by the DNS of others (see, for instance, [23,29,31,33]).

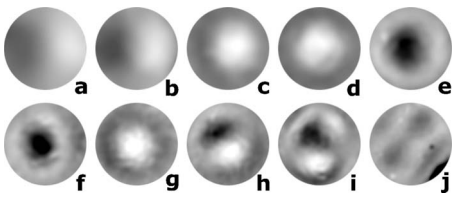

FIG. 5. Patterns at fixed $\varepsilon=0.1$ for various aspect ratios from sample W2. Values of Γ are (a) 1.00, (b) 1.33, (c) 1.66, (d) 2.00, (e) 2.33, (f) 2.67, (g) 3.00, (h) 3.33, (i) 3.66, and (j) 4.00.

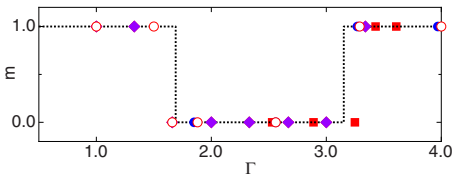

FIG. 6. (Color online) Mode number m of the pattern that formed just above the onset of convection as a function of the aspect ratio Γ. Solid circles (blue): sample W1a. Solid squares (red): sample W1b. Solid diamonds (purple online): sample W2. Open circles (red online): DNS. Dotted line: The mode with the lowest $\mathrm{Ra}_c^{\mathrm{LSA}}$ from Ref. [24] for a side-wall admittance $C=3.3$.

At somewhat larger Γ [Figs. 5(c)–5(g) for cells W2–4 to W2–8], the pattern corresponded to $m=0$ (a one torus in the Borońska and Tuckerman notation). Again, in this Γ range, the $m=0$ mode was found as well by our DNS and by the DNS of others (see, for instance, [23,31,36,43]).

The observed mode numbers, both in the experiment and in our DNS, are shown as a function of Γ in Fig. 6. One sees a well-defined transition from $m=1$ to $m=0$ as Γ increases. It occurs at a codimension-two point located at $\Gamma_{\mathrm{CD2}}^{(1)}=1.58\pm0.10$. We took the value 1.58 as the average of the two nearest points ($m=1$ at $\Gamma=1.50$ from DNS and $m=0$ at $\Gamma=1.66$ from cell W2–8) and the uncertainty as half the difference between these two Γ values, plus 0.02 to allow for possible systematic errors in Γ (see the last paragraph of Sec. II A).

The result for $\Gamma_{\mathrm{CD2}}^{(1)}$ can be compared to the value obtained by Buell and Catton from LSA. Their data for a sidewall admittance of $C=3.3$ yield $\Gamma_{\mathrm{CD2}}^{(1)}=1.69$. This result is slightly larger than our value, but there is considerable uncertainty about the sidewall admittance appropriate for comparison to experiment. Although in the LSA $\Gamma_{\mathrm{CD2}}^{(1)}$ is not very sensitive to the precise value of C, a somewhat smaller LSA value of C, say near 2.9, would yield a result for $\Gamma_{\mathrm{CD2}}^{(1)}$ near the upper limit of the experimental result. Thus we conclude that there is no real conflict between the LSA and the experiment.

We note that for $m=0$, there are two modes, one with up flow [Figs. 5(e) and 5(f), cells W2–6 and W2–5] and the other with down flow [Figs. 5(c), 5(d), and 5(g), cells W2–8, W2–7, and W2–4] in the cell center. In the ideal system, these two patterns would be degenerate, but one would expect small deterministic imperfections to break this degeneracy in the physical system. Consistent with this expectation, repeated runs suggest (even though our statistics are limited) that the same mode appears every time in a given cell rather than the selection being random.

As Γ increased further, beyond $\Gamma_{\mathrm{CD2}}^{(2)}=3.26\pm0.02$, the $m=1$ mode once more was the one that formed at onset [see Fig. 5(h), cell W2–3]. This is consistent with LSA [24] as well as with several DNS investigations [35,37,39] The second codimension-two point was determined more precisely by the data than was the first. We take it as the average Γ value of cells W1b-8 and W1a-9. The uncertainty of its location is essentially determined by the possible systematic errors of Γ (see the last paragraph of Sec. II A) and roughly we estimate it to be ±0.02.

Again we can compare our result for $\Gamma_{\mathrm{CD2}}^{(2)}$ to that of the LSA. The marginal curves of Buell and Catton [24] yield

FIG. 7. Patterns for $\Gamma=6.07$, sample W1a-5, for (from left to right) $\varepsilon=0.06$, 0.11, and 0.30. The bright dot near the top of each image is an imperfection in the optics.

$\Gamma^{(2)}_{CD2}=3.15$ for a sidewall admittance of 3.3. This is somewhat smaller than the experimental value 3.26 ± 0.02. It turns out that the LSA result for $\Gamma^{(2)}_{CD2}$ is almost independent of C. Thus, it seems difficult to reconcile the experimental and theoretical results. On the other hand, given the complexity of the marginal curves for the two modes, one might regard the agreement between experiment and LSA to be quite satisfactory.

As Γ increased even further, the observed modes became more complicated as seen in Figs. 5(i) and 5(j), cells W2–2 and W2–1. These patterns are not always easily described in terms of simple azimuthal Fourier modes. At the largest $\Gamma=4.00$ of sample W2 (W2–1), the structure very close to onset corresponded to $m=2$ in some runs and to $m=1$ in others, but with increasing ε it soon evolved into a pattern dominated by parallel rolls as seen in Fig. 5(j). The $m=2$ mode was observed very close to onset also at the similar $\Gamma=4.67$ in sample W1a-7. We note that, for $\Gamma=4$, LSA [24] and DNS [37,39] show that $m=1$ is the mode with the smallest Ra_c, but that at a Rayleigh number only about 1% higher the $m=2$ mode evolved from the conduction state. Thus it seems not surprising that the experiment yields one or the other, depending on particular detailed history.

At even larger $\Gamma\simeq6$, an $m=4$ mode was observed close to onset for cell W1a-5 as shown in Fig. 7. As seen in the figure, with increasing ε, this pattern evolved into one of parallel rolls. In the experiment, it seemed that this pattern evolution was gradual; however, since it involved a reduction of the symmetry of the pattern, one expects it to originate at a bifurcation [46] which was not explicitly resolved in the experiment. The observed pattern sequence with increasing Ra is quite similar to the one found from DNS by Borońska and Tuckerman (see Fig. 5 of [39]).

In Table I, we listed the mode numbers observed close to onset for all of our samples. A question mark shows that a clear identification was not possible and a number followed by r indicates that the preceding number gives the number of more or less parallel rolls that formed, within our resolution, immediately above onset. One sees that parallel rolls prevailed roughly for $\Gamma\gtrsim6$. This result agrees with the experimental findings of Kirchartz *et al.* [14] who observed parallel rolls under quasistatic conditions for $\Gamma=6$ and 6.8 and the DNS of Rüdiger and Feudel [34] for $\mathrm{Pr}=1$ and $\Gamma=8.0$.

Finally, we compare our patterns more explicitly to the experimental findings of others. Our observations of $m=1$ for $\Gamma\leq\Gamma^{(1)}_{CD2}$ and of $m=0$ for $\Gamma^{(1)}_{CD2}<\Gamma<\Gamma^{(2)}_{CD2}$ agree with the experiments of Müller *et al.* Our results are only partially in agreement with those reported by Stork and Müller [22] in their Fig. 2. SM made determinations of the patterns close to onset but did not specify the precise values of ε. For

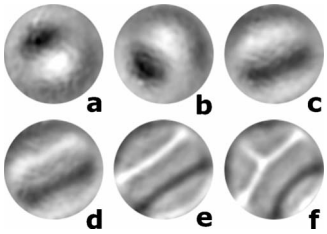

FIG. 8. Patterns for $\Gamma=3.34$, cell W2–3, at several ε values: (a) 0.09, (b) 0.22, (c) 0.34, (d) 1.19, (e) 3.87, (f) 4.84.

$\Gamma=1.6$ [their Fig. 2(a)], they found a pattern that could reasonably be interpreted as corresponding to $m=1$. Although this Γ value is quite close to $\Gamma^{(1)}_{CD2}$, this can be regarded as consistent with our results. However, after longer equilibration at the same Γ and with ε in the range of 0.05–0.1, their pattern evolved to an $m=2$ state [their Fig. 2(b)], which we did not observe at any ε in this Γ range. Consistent with our results, SM found a concentric roll ($m=0$) for $\Gamma=2.2$ [their Fig. 2(c)]. For $\gamma=3.2$ [their Fig. 2(d)], where our work yielded $m=0$, they already found a state consisting of three parallel rolls. The smallest Γ value at which we found parallel rolls was 5.37 (cell W1a-6, Table I). Thus, even their result for $\Gamma=4.4$ [their Fig. 2(e)] is inconsistent with our work. For larger Γ, their observations of more or less parallel rolls at $\Gamma=5.6$ [their Fig. 2(f)] and $\Gamma=6.4$ [their Fig. 2(g)] are consistent with our results, as well as with those of Kirchartz *et al.* for $\Gamma=6$ and 6.8. It is difficult to be sure about the reason for the differences between the patterns found by SM and by us. Reasons that come to mind may include different equilibration times, different increments of ΔT, and perhaps larger values of ε.

C. Patterns further above onset

Here we consider some examples of what happens to the patterns as ε is increased well above zero. In Fig. 8, we see that, for $\Gamma=3.34$, cell W2–3, the $m=1$ mode that forms at onset persists up to about $\varepsilon=0.3$, but with further increase the up-flow and down-flow regions broaden gradually and expand into a parallel roll pair as seen in Figs. 8(c)–8(e). There is no evidence of any instability with respect to $m=0$ or larger m values. This result is similar to those of Borońska and Tuckerman, Fig. 14 of [39] and Fig. 23 of [38], who found $m=1$ just above onset and a gradual evolution to a roll state as Ra increased. At even larger ε, side-wall influence causes the formation of more complex patterns as shown in Fig. 8(f).

At the slightly smaller $\Gamma=3.25$ represented by cell W1b-8, the $m=0$ mode (a concentric roll) formed at onset, but at $\varepsilon\simeq0.07$ there was a secondary bifurcation, clearly visible as a discontinuity of the variance $\sigma(\varepsilon)$ as well as in the images, to $m=1$. This is shown in Fig. 9. It suggests that there is a bifurcation line, presumably starting at the codimension-two point at $\Gamma\simeq3.26$, and extending quite steeply but to smaller Γ as ε increases.

In Fig. 10, we see that for $\Gamma=2.33$, cell W2–6, the $m=0$ mode persisted up to the largest $\varepsilon=3.29$ studied, but that there was a transition near $\varepsilon=0.07$ from down flow to up

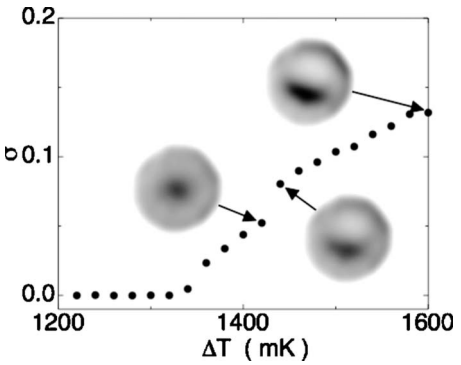

FIG. 9. Variance as a function of ΔT for $\Gamma=3.25$, cell W1b-8. Images of the patterns are shown for $\Delta T=1420$, 1440, and 1600 mK, corresponding to $\varepsilon=0.059$, 0.074, and 0.19 respectively.

flow in the cell center. This is surprising since a significant perturbation is expected to be required to cause a transition between these two stable states.

In Fig. 11 for $\Gamma=1.66$, cell W2–8, one sees that the $m=0$ mode that formed at onset persisted up to $\varepsilon=0.33$, but then underwent a change to a pattern of lower symmetry that is difficult to characterize in terms of simple azimuthal Fourier modes. For $\Gamma=1.00$, cell W2–10, a pattern corresponding to $m=1$ persisted up to $\varepsilon\simeq 1.0$, which was the largest value we investigated.

IV. DIRECT NUMERICAL SIMULATIONS

To solve the Boussinesq equations numerically, we used the code NEK5000 [44], a parallel, spectral element code developed to solve the Navier-Stokes equations. We used a time resolution of $0.002\tau_v$ (where $\tau_v \equiv L^2/\kappa$ is a vertical thermal diffusion time) and a spatial resolution of about 0.1 times the depth of the cell. The numerical code had been thoroughly checked for these systems in Ref. [45]. As shown on pages 18 to 19 of that reference, convergence in both the space and time domains was demonstrated for $\Gamma=4$ and $\sigma=0.78$, which is very close to the parameter regime studied here. For each simulation, the initial conditions were random, with an amplitude of 0.001 (in scaled temperature units). We used the same initial conditions for each Γ value, but the initial conditions did vary with Γ, since the numerical grids were different. We used both insulating and conducting sidewalls. In all cases, the simulations were evolved until the Nusselt number no longer changed within our resolution over a time period of ten horizontal diffusion times, i.e., over a period of $10\Gamma^2\tau_v$. We used a Prandtl number of 28.9 to agree with the experiments and varied our aspect ratio from $\Gamma=1$ to $\Gamma=4$. The critical Rayleigh number $\mathrm{Ra}_c^{\mathrm{DNS}}$ was determined by extrapolating to zero the Nusselt number as a function of Ra.

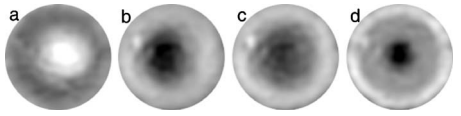

FIG. 10. Patterns for $\Gamma=2.33$, cell W2–6, at (a) $\varepsilon=0.05$, (b) $\varepsilon=0.09$, (c) $\varepsilon=0.72$, and (d)$\varepsilon=3.29$.

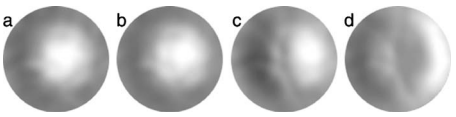

FIG. 11. Patterns for $\Gamma=1.66$, cell W2–8, at (a) $\varepsilon=0.12$, (b) $\varepsilon=0.33$, (c) $\varepsilon=0.37$, and (d) $\varepsilon=1.66$.

Results for $\mathrm{Ra}_c^{\mathrm{DNS}}$ are given in Table II for both insulating and conducting lateral walls. There they are compared to the marginal curve $\mathrm{Ra}_c^{\mathrm{LSA}}$ obtained from LSA [24]. Considering that the values of $\mathrm{Ra}_c^{\mathrm{LSA}}$ had to be read off low-resolution graphs, the agreement is as good as can be expected. Agreement between $\mathrm{Ra}_c^{\mathrm{DNS}}$ and $\mathrm{Ra}_c^{\mathrm{LSA}}$ should prevail if the bifurcations are supercritical.

Just above onset, we find patterns that agree well with those observed in the experiment. Some are shown in Fig. 12 and their azimuthal mode (m) and radial node numbers (n) are given in Table II. The results for m of the patterns just above onset for conducting boundaries are shown also in Fig. 6. They are seen to agree well with the experimental results as well as with the prediction from LSA of the lowest mode that acquires a positive growth rate. When we compare m for both insulating and conducting boundary conditions to the LSA results [24], we also obtain good agreement.

From the DNS, we can identify not only the azimuthal mode number m, but also the number of radial nodes n for these patterns. Here, we take n as the number of zero cross-

TABLE II. Results for the critical Rayleigh number $\mathrm{Ra}_c^{\mathrm{DNS}}$ from this work, the critical Rayleigh number $\mathrm{Ra}_c^{\mathrm{LSA}}$ from the linear stability analysis of Ref. [24], the mode numbers (m,n) found near onset, and the corresponding smallest $\varepsilon^{\mathrm{DNS}} \equiv \mathrm{Ra}/\mathrm{Ra}_c^{\mathrm{DNS}} - 1$ values at which computations were carried out as a function of Γ for $\sigma=28.9$. Sidewalls are insulating (first data set) or conducting (second data set) and initial conditions are random. Near onset, m indicates the azimuthal mode and n indicates the radial node number as defined in the text.

Γ	$\mathrm{Ra}_c^{\mathrm{DNS}}$	$\mathrm{Ra}_c^{\mathrm{LSA}}$	$10^3\varepsilon^{\mathrm{DNS}}$	(m,n)
		Insulating		
1	3768	4100	8	1,0
1.5	2586	2600	5	1,0
1.88	2441	2400	4	0,1
2.56	1906	1900	5	0,1
3.29	1869	1850	16	1,1
		Conducting		
1	8000	7800	6	1,0
1.5	3966	4100	9	1,0
1.66	3326	3400	7	0,1
1.88	2750	2800	4	0,1
2.56	2100	2100	6	0,1
3.29	1961	1950	7	1,1
4	1879	1900	4	1,1

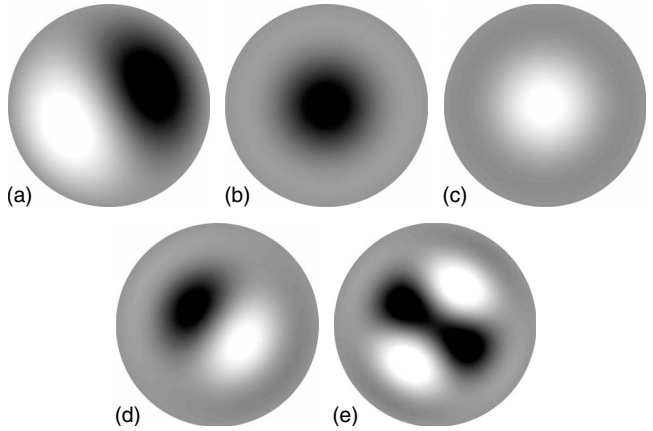

FIG. 12. Patterns obtained from DNS for $\sigma=28.9$. (a) $\Gamma=1$, $\varepsilon=0.006$. (b) $\Gamma=1.66$, $\varepsilon=0.007$. (c) $\Gamma=1.66$, $\varepsilon=0.019$. (d) $\Gamma=3.29$, $\varepsilon=0.007$. (e) $\Gamma=4$, $\varepsilon=0.03$. In all cases, conducting lateral boundary conditions were used.

ings along a radius r of the deviation Θ of the temperature field from the conduction profile, but we exclude the trivial ones at $r=0$ and at $r=D/2$. The radial structure of some of the patterns is illustrated in Figs. 13 and 14. The onset pattern for the lowest Γ values [Figs. 12(a), 13(a), and 14(a)] is an $m=1$ mode, with no radial nodes ($n=0$). Thus, this example corresponds to $(m,n)=(1,0)$. As Γ increases, the onset pattern changes to an $m=0$ mode as seen in Figs. 12(b), 12(c), 13(b), and 14(b). In this case, there is one off-axis radial node, so we denote this as (0,1). We note that for $m=0$, the $n=1$ node is the lowest possible one that allows mass conservation. Finally, as Γ increases further, we return again to an $m=1$ azimuthal mode as seen in Figs. 12(d), 13(c), and 14(c). However, in this case, there is one off-axis

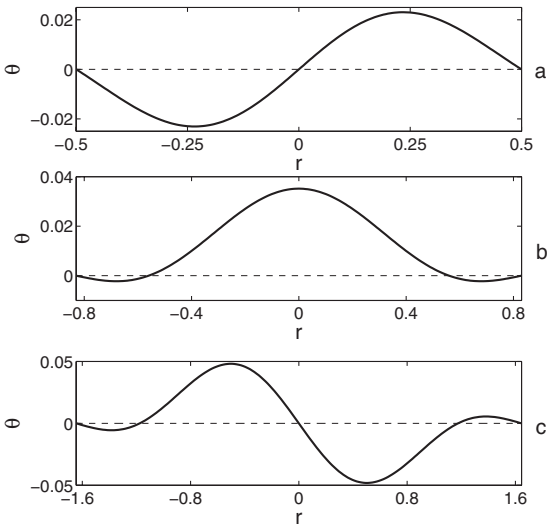

FIG. 13. Radial profiles ($y=0$) of the temperature deviation field $\theta=T-0.5$ at the midplane ($z=0.5$) for different Γ values and conducting lateral boundary conditions (in the plane of Fig. 12, the x axis is horizontal and the y axis is vertical). (a) $\Gamma=1$, $\varepsilon=0.006$, Fig. 12(a). (b) $\Gamma=1.66$, $\varepsilon=0.007$, Fig. 12(b). (c) $\Gamma=3.29$, $\varepsilon=0.007$, Fig. 12(d). The corresponding profiles for insulating boundary conditions are similar.

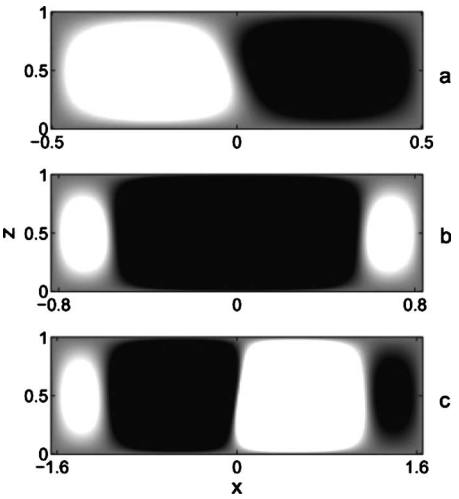

FIG. 14. Grayscale plots of the temperature deviation field $\theta=T-(1-z)$ for the $z-x$ plane at $y=0$ for the three different Γ values of Fig. 13 and conducting boundary conditions. The thresholding is purposefully made very small to highlight the interior radial nodes. (a) $\Gamma=1$, $\varepsilon=0.006$, $\theta_m=0.023$ (maximum magnitude of θ). (b) $\Gamma=1.66$, $\varepsilon=0.007$. $\theta_m=0.035$, but the magnitude of the second peak at $x=\pm 0.7$ is $\theta_s=0.002$. (c) $\Gamma=3.29$, $\varepsilon=0.007$, $\theta_m=0.048$, $\theta_s=0.006$ at $x=\pm 1.4$. Similar profiles exist for insulating boundary conditions.

radial node, so we denote it as (1,1). Here we note that for $m=1$, the $n=0$ node is allowed, as illustrated by Figs. 12(a), 13(a), and 14(a). It is not surprising that different radial nodes will occur at onset as Γ increases. Indeed, this phenomenon is evident already from the early stability analysis of Charlson and Sani [26]. Hence, we would expect higher radial nodes as Γ is increased. Our experiment did not have adequate contrast to resolve any radial nodes.

We also included an $m=2$ pattern in Fig. 12(e), although this was not the onset pattern. However, these higher m patterns are present in our simulations at higher ε in agreement with the experiments as in Fig. 7.

The $m=0$ mode is interesting since the center region can have either up flow or down flow. We almost always observed down flow in the center region and did not observe any transition to an up-flow state as ε was increased. We did observe an up-flow onset state for $\Gamma=1.66$ and conducting sidewalls. In this case, as ε was increased, the simulation once more yielded a down-flow state as seen in Figs. 12(b) and 12(c). Finally, no evidence of a subcritical bifurcation or an imperfect bifurcation was found in the DNS.

V. SUMMARY

We reported on an experimental and numerical investigation of the onset of convection in cylindrical samples with circular cross sections and with aspect ratios $1 \lesssim \Gamma \lesssim 9$. In the experiment, we used three separate samples, each containing several cells with different Γ. The numerical work consisted of DNS of the Boussinesq equations.

We obtained values of Ra_c by extrapolating pattern variances (in the experiment) or Nusselt numbers (in the DNS)

back to the value in the conduction state. These results are in good agreement with the linear stability analysis of Buell and Catton [24] which takes the finite conductivity of side walls into account.

The patterns near onset and the ranges of Γ over which they were found were reasonably consistent with the stability analysis (LSA) of Buell and Catton [24] and agreed with several DNS investigations [23,29,31–34,36,38,39]. For $\Gamma \leq \Gamma_{CD2}^{(1)} = 1.58 \pm 0.10$, we found a single convection roll, corresponding to an azimuthal Fourier mode with $m=1$. For comparison, the codimension-two point based on the crossing of the neutral curves obtained from LSA occurred at $\Gamma = 1.69$, a value slightly larger than the experiment. For $\Gamma_{CD2}^{(1)} \leq \Gamma \leq \Gamma_{CD2}^{(2)} = 3.26 \pm 0.02$, a concentric roll (or torus), corresponding to $m=0$, was observed. The LSA yielded $\Gamma_{CD2}^{(2)} = 3.15$, which is somewhat smaller than the experimental value. For Γ somewhat larger than $\Gamma_{CD2}^{(2)}$, the pattern once more corresponded to $m=1$, but our DNS showed that, compared to the $m=1$ mode at small Γ, there was an additional radial node. This feature could not be resolved in the experiment. As Γ increased further, more complicated patterns were observed, including ones corresponding to $m=2$ and $m=4$. For $\Gamma \gtrsim 5$ or so, there was a tendency to form parallel rolls even very close to or at onset.

We also report on more limited results for the pattern evolution as Ra is increased well beyond Ra_c. For $\Gamma = 3.25 < \Gamma_{CD2}^{(2)}$, where an $m=0$ mode formed at onset, a secondary bifurcation to $m=1$ was observed near $\mathrm{Ra}/\mathrm{Ra}_c = 1.1$. For $\Gamma = 3.34 > \Gamma_{CD2}^{(2)}$, the $m=1$ pattern that formed at onset evolved gradually into a pattern consisting of a straight-roll pair. A similar evolution was observed by DNS for $\Gamma=4$ and $\mathrm{Pr} = 6.7$ by Borońska and Tuckerman [39].

Although our experiments and those of others [14,22,23] have provided a fairly detailed overall picture of the pattern-formation phenomena close to onset in this system, there remain some unresolved issues. One of them pertains to the radial structure of the $m=1$ patterns above $\Gamma_{CD2}^{(2)}$. Although our DNS (and those of others) resolved a radial node not present at smaller Γ, our experiment was unable to resolve this feature. A more detailed experimental investigation with higher resolution and over wider parameter ranges should be carried out.

Another feature that might be studied in more detail is the secondary bifurcation line from $m=0$ to $m=1$ that was observed by the experiment for $\Gamma = 3.25$ (see Fig. 9). Presumably, this line originates at $\Gamma_{CD2}^{(2)}$ and then slopes toward smaller Γ as Ra increases. The nature of this bifurcation also has not been studied; presumably it is subcritical and there should be some hysteresis. Of course, there also is much more to be learned about the range $\Gamma \gtrsim 5$ where more complicated patterns will form, but there the various marginal stability curves [24] are so close together that it will be very difficult to develop an unambiguous picture from experiment.

An issue of particular interest is how, as a function of Γ, the pattern very near onset changes from one described by azimuthal Fourier modes to one consisting of parallel rolls. If the parallel rolls form via a secondary bifurcation, then the dependence of the corresponding $\mathrm{Ra}_c^{(2)}$ on Γ would be of interest. If, on the other hand, the transition to rolls is gradual, as seems possible only in the dipolar ($m=1$) case shown in Fig. 8, then one would like to know the Γ dependence of the characteristic Rayleigh range for that evolution. Presumably, either that range or $\mathrm{Ra}_c^{(2)}$ would approach Ra_c as Γ becomes large. And, of course, as Ra is increased further, the richness of phenomena (see, for instance, [25,39] and numerous additional DNSs) seems without limit.

ACKNOWLEDGMENTS

We are grateful to Eric Brown, James Hogg, and Tal Sharf for their assistance with the experiment. We also appreciate discussions with and constructive remarks by Mike Cross and Laurette Tuckerman. The experimental work was supported by the U.S. National Science Foundation through Grant No. DMR07-02111. The numerical work was supported in part by the U.S. National Science Foundation through Grant No. PHY05-51164.

[1] H. Bénard, Rev. Gen. Sci. Pures Appl. **11**, 1261 (1900); **11**, 1309 (1900).
[2] H. Bénard, Ann. Chim. Phys. **23**, 62 (1901).
[3] E. Bodenschatz, W. Pesch, and G. Ahlers, Annu. Rev. Fluid Mech. **32**, 709 (2000).
[4] L. Rayleigh, Philos. Mag. **32**, 529 (1916).
[5] H. Jeffreys, Proc. R. Soc. London, Ser. A **118**, 195 (1928).
[6] L. Lorenz, Ann. Phys. Chem. **13**, 581 (1881).
[7] D. Joseph, J. Fluid Mech. **47**, 257 (1971).
[8] J. R. de Bruyn, E. Bodenschatz, S. W. Morris, S. Trainoff, Y. Hu, D. S. Cannell, and G. Ahlers, Rev. Sci. Instrum. **67**, 2043 (1996).
[9] A. Schlüter, D. Lortz, and F. 2Busse, J. Fluid Mech. **23**, 129 (1965).
[10] K. M. S. Bajaj, N. Mukolobwiez, N. Currier, and G. Ahlers, Phys. Rev. Lett. **83**, 5282 (1999).
[11] N. M. Ercolani, R. Indik, A. Newell, and T. Passot, J. Nonlinear Sci. **10**, 223 (2000).
[12] W. Meevasana and G. Ahlers, Phys. Rev. E **66**, 046308 (2002).
[13] E. L. Koschmieder and S. G. Pallas, Int. J. Heat Mass Transfer **17**, 991 (1974).
[14] K. R. Kirchartz, U. Müller, H. Oertel, and J. Zierep, Acta Mech. **40**, 181 (1981).
[15] V. Croquette, M. Mory, and F. Schosseler, J. Phys. (France) **44**, 293 (1983).
[16] V. Steinberg, G. Ahlers, and D. S. Cannell, Phys. Scr. **32**, 534 (1985).
[17] G. Ahlers, D. S. Cannell, and V. Steinberg, Phys. Rev. Lett. **54**, 1373 (1985).
[18] M. S. Heutmaker, P. N. Fraenkel, and J. P. Gollub, Phys. Rev. Lett. **54**, 1369 (1985).
[19] V. Croquette, Contemp. Phys. **30**, 113 (1989).

[20] V. Croquette, Contemp. Phys. **30**, 153 (1989).
[21] E. Bodenschatz, J. R. deBruyn, G. Ahlers, and D. S. Cannell, Phys. Rev. Lett. **67**, 3078 (1991).
[22] K. Stork and U. Müller, J. Fluid Mech. **71**, 231 (1975).
[23] G. Müller, G. Neumann, and W. Weber, J. Cryst. Growth **70**, 78 (1984).
[24] J. C. Buell and I. Catton, ASME J. Heat Transfer **105**, 255 (1983).
[25] B. Hof, P. G. J. Lucas, and T. Mullin, Phys. Fluids **11**, 2815 (1999).
[26] G. S. Charlson and R. L. Sani, Int. J. Heat Mass Transfer **13**, 1479 (1970).
[27] G. S. Charlson and R. L. Sani, Int. J. Heat Mass Transfer **14**, 2157 (1971).
[28] G. S. Charlson and R. L. Sani, J. Fluid Mech. **71**, 209 (1975).
[29] M. Wanschura, H. C. Kuhlmann, and H. J. Rath, J. Fluid Mech. **326**, 399 (1996).
[30] G. Hardin, R. Sani, D. Henry, and B. Roux, Int. J. Numer. Methods Fluids **10**, 79 (1990).
[31] G. Neumann, J. Fluid Mech. **214**, 559 (1990).
[32] F. Marques, M. Net, J. M. Massaguer, and I. Mercader, Comput. Methods Appl. Mech. Eng. **110**, 157 (1993).
[33] R. Touihri, H. Ben Hadid, and D. Henry, Phys. Fluids **11**, 2078 (1999).
[34] S. Rüdiger and F. Feudel, Phys. Rev. E **62**, 4927 (2000).
[35] S. Leong, Numer. Heat Transfer, Part A **41**, 673 (2002).
[36] K. Borońska and L. S. Tuckerman, J. Fluid Mech. **559**, 279 (2006).
[37] D. J. Ma, D. J. Sun, and X. Y. Yin, Phys. Rev. E **74**, 037302 (2006).
[38] K. Borońska and L. S. Tuckerman, Phys. Rev. E **81**, 036320 (2010).
[39] K. Borońska and L. S. Tuckerman, Phys. Rev. E **81**, 036321 (2010).
[40] G. Ahlers, D. S. Cannell, L. I. Berge, and S. Sakurai, Phys. Rev. E **49**, 545 (1994).
[41] T. Daubert and R. Danner, *Physical and Thermodynamic Properties of Pure Chemicals* (Hemisphere Publishing Corporation, New York, 1989).
[42] G. Ahlers and X. Xu, Phys. Rev. Lett. **86**, 3320 (2001).
[43] G. Hardin and R. Sani, Int. J. Numer. Methods Fluids **17**, 755 (1993).
[44] P. F. Fischer, J. Comput. Phys. **133**, 84 (1997).
[45] J. Scheel, Ph.D. thesis, California Institute of Technology, 2006; http://thesis.library.caltech.edu/3217/
[46] This was called to our attention by Laurette Tuckerman.